# A model for surface tension in the finite volume particle method without parasitic current

Mohsen H. Moghimi and Nathan J. Quinlan
Mechanical Engineering and CÚRAM Centre for Research in Medical Devices
National University of Ireland Galway
Galway, Ireland
m.hassanzadehmoghimi1@nuigalway.ie

***Abstract*— A surface tension model has been developed in the finite volume particle method (FVPM). Surface tension force is applied only on free-surface particles, which are inexpensively and robustly detected using the FVPM definition of interparticle area. We present a simple model in which the direction of the pairwise surface tension force is approximated by the common tangent of free-surface particle supports. The method is validated in 2D for formation of an equilibrium viscous drop from square and elliptical initial states, drops on hydrophobic and hydrophilic walls, and impact of a small cylinder on a liquid surface. Results are practically free from parasitic current associated with inaccurate curvature determination in some methods.**

## I. INTRODUCTION

In this article we describe a simple new model for surface tension in the finite volume particle method (FVPM), with the aim of improving accuracy, and in particular eliminating the spurious or parasitic velocity which is a feature of many surface tension models in both mesh-based and meshless methods. We show validation of the method in 2D static and dynamic problems. In mesh-based computational fluid dynamics, the accurate determination of interfaces, with or without surface tension, is not straightforward because interfaces do not generally conform to the mesh. In particle methods, in contrast, the computational nodes or particles are free to move, making it trivial in principle to track the surface of the fluid. In addition, FVPM in particular allows definitive identification of particles at the free surface, greatly simplifying the implementation of surface tension models.

FVPM is a relatively novel numerical technique in computational fluid dynamics, introduced by Hietel *et al.* in 2000 [1]. It preserves the conservative flux-based formulation of the classical finite volume method (FVM), along with the Lagrangian nature of meshless particle methods such as smoothed particle hydrodynamics (SPH), which is advantageous for moving boundary and free-surface problems.

Particle methods to simulate surface tension may be categorized as microscopic or macroscopic. Microscopic methods in SPH are based on application of van der Waals (vdW)-like potentials or other attractive-repulsive forces between particles [2,3,4]. The surface tension coefficient does not appear explicitly, and consequently the model requires calibration of coefficients. Van der Waals-based models are also sensitive to temperature. The macroscopic continuum surface force (CSF) model was proposed by Brackbill *et al.* [5] for the FVM. Morris [6], Muller *et al.* [7], Liu *et al.* [8], Adami *et al.* [9], Breinlinger *et al.* [10], and Schnabel *et al.* [11] applied the technique in SPH. In this method, the surface tension force is a function of the surface tension coefficient, local curvature of the interface, and the local surface normal. Interface curvature and normals are computed from gradients of a color function which varies across the interface. The method is sensitive to the numerical calculation of gradients of the color function.

Maertens *et al.* [12,13] introduced surface tension modelling in FVPM. They simulated 3D drops in isolation and interacting with solid surfaces, using the physical surface tension coefficient, without explicitly estimating the curvature of the interface or tuning any parameters. This is possible in FVPM because free-surface particles can be identified unambiguously and the free surface itself is well-defined in terms of the particle geometry. In this technique, the surface tension force is calculated at the intersection curves of spherical particles on the free surface. However, the method suffers from some resolution-dependent spurious velocity.

In this paper, a variant model for surface tension in FVPM is presented. Section 2 summarizes the FVPM formulation for fluid flow computations. In section 3, the new surface tension model in FVPM is described. In section 4, numerical results are presented and discussed.

## II. GOVERNING EQUATONS

### A. Governing Equations

The Navier-Stokes equations without source terms can be written in conservation form as

$$\frac{\partial \mathbf{U}(t\,,\mathbf{x})}{\partial t}+\nabla\,.\,\mathbf{F}\left(\mathbf{U}(t\,,\mathbf{x})\right)=0\,, \tag{1}$$

$$\mathbf{U}=\begin{Bmatrix}\rho\\ \rho\mathbf{u}\end{Bmatrix}\,, \tag{2}$$

$$\mathbf{F}=\begin{Bmatrix}\rho\mathbf{u}\\ \rho\mathbf{u}\mathbf{u}+p\mathbf{I}-\boldsymbol{\tau}\end{Bmatrix}\,, \tag{3}$$

where $\mathbf{U}(t\,,\mathbf{x})$, $\mathbf{F}$, $t$, and $\mathbf{x}$ represent the vector of conserved quantities, flux functions, time, and position, respectively. In the conserved quantities and flux functions, $\rho$, $\mathbf{u}$, $p$, $\mathbf{I}$, and $\boldsymbol{\tau}$ are density, velocity, pressure, identity tensor, and viscous stress

tensor of the fluid, respectively. Equation (4) is used for pressure calculation:

$$p = \frac{\rho_0 c_0^2}{\gamma}\left[\left(\frac{\rho}{\rho_0}\right)^{\gamma} - 1\right], \tag{4}$$

where $\rho_0$, $c_0$, and $\gamma$ are reference density of the fluid, reference sound speed, and a constant, respectively. The value of $\gamma$ is set to 7 in the present work.

### B. Numerical Model

The FVPM formulation of (1) for particle $i$ is

$$\frac{\mathrm{d}}{\mathrm{d}t}\left(\mathbf{U}_i(t)V_i(t)\right) = -\sum_{j=1}^{N} \boldsymbol{\beta}_{ij} \cdot \left[\mathbf{F}\left(\mathbf{U}_{ij}\right)(t, \mathbf{x}) - \mathbf{U}_{ij}(t, \mathbf{x})\, \dot{\mathbf{x}}_{ij}(t)\right] - \int \Psi_i(t, \boldsymbol{x})\mathbf{F}\left(\mathbf{U}_{ij}\right)(t, \mathbf{x}) \cdot d\mathbf{S}, \tag{5}$$

where $N$, $V_i$, $\boldsymbol{\beta}_{ij}$, $\mathbf{U}_{ij}(t)$, $\dot{\mathbf{x}}_{ij}$, $\Psi_i$, and $d\mathbf{S}$ are the number of neighbours of particle $i$, particle volume, interparticle area vector between particles $i$ and $j$, vector of conserved quantities at the interface of particles $i$ and $j$, velocity of the interface, test function of the particle, and the surface area vector of the support of particle $i$, respectively. Both the flux and the interface velocity depend on the particle transport velocity $\dot{\boldsymbol{x}}_i$, which can be chosen arbitrarily. In the present work, we set $\dot{\mathbf{x}}_i = \mathbf{u}_i$, i.e. a purely Lagrangian model. The interparticle area is defined as:

$$\boldsymbol{\beta}_{ij} = \boldsymbol{\gamma}_{ij} - \boldsymbol{\gamma}_{ji}, \tag{6}$$

where

$$\boldsymbol{\gamma}_{ij} = \int \Psi_i(t, \mathbf{x}) \frac{\nabla W_j(t, \mathbf{x})}{\sigma(t, \mathbf{x})} d\mathbf{x}, \tag{7}$$

In the above, $W_j$, $\sigma$ and $\Psi_i$ are the kernel function, kernel summation and test function, respectively, defined as follows:

$$W_i(t, \mathbf{x}) = m_i\, W(\mathbf{x} - \mathbf{x}_i(t), h), \tag{8}$$

$$\sigma(t, \mathbf{x}) = \sum_{j=1}^{N} W_j(t, \mathbf{x}), \tag{9}$$

$$\Psi_i(t, \mathbf{x}) = \frac{W_i(t, \mathbf{x})}{\sigma(t, \mathbf{x})}, \tag{10}$$

In (8), $m_i$ and $h$ are the particle's mass and the smoothing length of the kernel function, with compact support radius $2h$. To close the system of equations, the evolution of the particle volume is calculated using

$$\frac{\mathrm{d}}{\mathrm{d}t} V_i(t) = \sum_{i=1}^{N} \left(\boldsymbol{\gamma}_{ij} \cdot \dot{\mathbf{x}}_j(t) - \boldsymbol{\gamma}_{ji} \cdot \dot{\mathbf{x}}_i(t)\right), \tag{11}$$

where $V_i(t)$ is defined as $V_i(t) = \int \Psi_i(t, \mathbf{x})\mathrm{d}\mathbf{x}$. Interparticle inviscid fluxes of (3) are computed using the AUSM$^+$-up scheme [14]. For detailed derivation of the FVPM formulation and further discussion of the extension of FVPM to viscous flow, readers are referred to [15] and [16] respectively.

### C. Free-Surface Detection in FVPM

Neighbouring particles and their weight functions determine the interparticle area vectors $\boldsymbol{\beta}_{ij}$. As illustrated in Fig. 1, particles $j$, $k$, $m$, $n$, and $p$ are considered as the neighbours of particle $i$, because their compact supports overlap the compact support of particle $i$. If the boundary of a particle's support is fully covered by neighbouring particles (Fig. 1(a)), it can be shown from (6) and (7) that its area vectors sum to zero ($\sum_{j=1}^{N} \boldsymbol{\beta}_{ij} = 0$). In contrast, if the summation of the interaction vectors between the particle of interest and its neighbours is not equal to zero ($\sum_{j=1}^{N} \boldsymbol{\beta}_{ij} \neq 0$) it means that the particle is on the free surface (Fig. 1(b)).

In the present work, $W$ is defined as a top-hat function, and consequently $\boldsymbol{\beta}_{ij}$ can be calculated quickly and exactly [16].

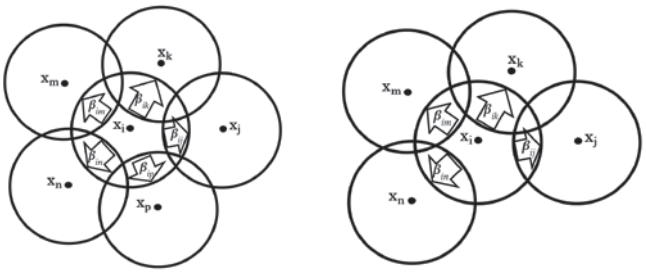


**Fig. 1.** Summation of interparticle area vectors between particle $i$ and its neighbours is (a) zero and (b) non-zero.

## III. New Model for Surface Tension in FVPM

### A. Surface Tension (Cohesion)

To calculate the surface tension force, the free-surface particles must be detected, and the appropriate force applied between particles. A free-surface particle pair is shown in Fig. 3. The cohesive surface tension force may be written as

$$\mathbf{F}^c = \sigma_{LV} l \mathbf{n}, \tag{13}$$

where $\sigma_{LV}$ and $l$ are the surface tension coefficient between liquid and gas and the length of the intersection curve of the particle surfaces (or unit out-of-plane length in 2D). The unit vector $\mathbf{n}$ is the direction of the surface tension force, which is to be determined. Particles $i$ and $j$ exert equal and opposite cohesion force $\mathbf{F}_{ij}$ on each other.

The direction of the force should be tangent to the free surface. In FVPM, the free surface is composed of the exposed surfaces of the particle support volumes, giving a bumpy approximation to the true free surface. The novel feature of the present work is to use the common tangent of particles $i$ and $j$ as an approximation for the free surface tangent. If the particles are of equal size, this is parallel to the centre-to-centre line. The general formula for cohesive force between particle $i$ and its $N$ neighbours is then

$$\mathbf{F}_i^c = \sum_{j=1}^{N} \sigma_{LV} l \mathbf{n}_{ij}, \tag{15}$$

where $\mathbf{n}_{ij}$ is defined as $\frac{\mathbf{x}_j - \mathbf{x}_i}{|\mathbf{x}_j - \mathbf{x}_i|}$. In contrast to other macroscopic methods, in FVPM the curvature need not be calculated explicitly.

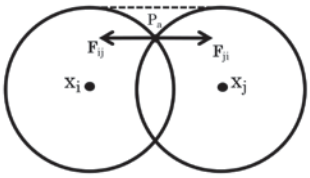


**Fig. 2.** Schematic view of surface tension force vectors between particle *i* and *j* (cohesive force) at point $P_a$, and the free-surface common tangent (dashed line) of the particles.

The proposed method differs from the approach of Maertens *et al*. [12,13], who derived the interparticle force in 3D by considering changes in surface energy of the particles' exposed spherical surface patches due to motion of the particles. This yields forces tangent to the particle support boundaries. For a pair of equally sized particles, the resulting force reduces to a centre-to-centre vector with a geometric correction factor.

### B. Surface Tension (Adhesion)

In the presence of a solid-liquid interface, the adhesive force is applied at the intersection point on the wall, point $P_f$. In Fig. 3, $\sigma_{LV}$, $\sigma_{SV}$, and $\sigma_{SL}$ are the surface tension coefficients of the liquid-gas interface, solid-gas interface, and solid-liquid interface respectively. Young's relation links these coefficients with the equilibrium contact angle $\theta_e$ as follows [17]:

$$\sigma_{SV} - \sigma_{SL} = \sigma_{LV} \cos(\theta_e) \,. \tag{16}$$

The normal components of the cohesive and adhesive force are in balance. Only the tangential components are responsible for the movement of the contact line. Defining the tangent vector of the wall as $\mathbf{n}_t$, the corresponding tangential component of adhesive force is written as

$$\mathbf{F}^a_{i,t} = \left( |\mathbf{F}^c_i| \cos(\theta_d) - \sigma_{LV} \cos(\theta_e) \right) \mathbf{n}_t \,, \tag{17}$$

where $\theta_d$ is defined as the instantaneous dynamic contact angle between the cohesive force vector and the wall.

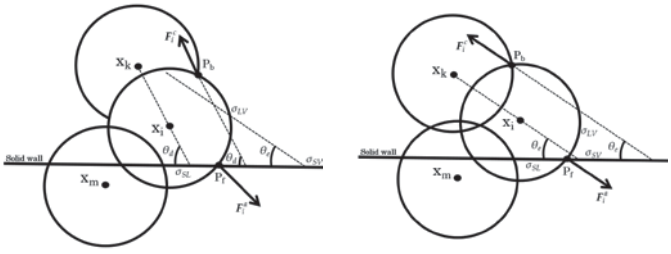


**Fig. 3.** Schematic diagram of surface tension force between particle *i* and a solid wall ($\mathbf{F}^a_i$) at point $P_f$ in (a) non-equilibrium (b) equilibrium state.

## IV. Numerical Resutls

The results of static and dynamic test cases are presented to show the accuracy and flexibility of the new surface tension model. The method is applied for initially square 2D droplets in free space and on a solid wall, as problems expected to result in static equilibrium. To test the method in strongly dynamic cases, we simulated oscillation of an elliptical drop and impact of a solid cylinder on a liquid surface.

### A. Initially Square 2D Liquid Droplet

The first test case is formation of a circular drop from an initial square distribution of liquid particles (Fig. 4) with surface tension coefficient $\sigma$, density $\rho$, and dynamic viscosity $\mu$. The Reynolds number based on the square's side length $L$ and characteristic velocity $\sigma/\mu$ changes from 0.3633 to infinity (inviscid fluid). The Ohnesorge number based on the square's side length $L$ is defined as $\mu/\sqrt{\rho\sigma L}$ and varies between 0 (inviscid fluid) and 0.166. The ratio $L/\Delta x$ is 25, where $\Delta x$ is the initial particle spacing.

In the absence of external forces, the initial square arrangement of the particles becomes a circular droplet through a sequence of oscillations. The evolution of the 2D viscous droplet is illustrated in Fig. 4. For an infinite, inviscid cylindrical drop, the period of small-amplitude oscillation is given by Rayleigh [2,18] as

$$\tau = 2\pi \sqrt{\frac{\rho R^3}{6\sigma}} \,. \tag{18}$$

The dimensionless time $t^*$ and radius $r_i^*$ are defined as $t/\tau$ and $|\mathbf{x}_i - \bar{\mathbf{x}}|/R$, where $\mathbf{x}_i$, $\bar{\mathbf{x}}$, and $R$ are particle's position, centre of mass position, and radius of the steady-state circular droplet.

Pressure error $\varepsilon_p$ is defined as $\frac{p_{NUM} - p_{AN}}{p_{AN}}$, where $p_{NUM}$ and $p_{AN}$ are the steady-state numerical and analytical pressure. The analytical internal pressure for an infinitely long cylindrical liquid drop under surface tension in zero ambient pressure is given by

$$p_{AN} = \frac{\sigma}{R} \,. \tag{19}$$

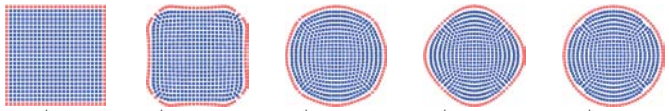


**Fig. 4.** Snapshots of 2D viscous liquid droplet evolution from an initial square shape, $L/\Delta x$=25 (red points are free-surface particles).

Fig. 5 shows the distribution of error in computed pressure across the drop in its final condition. The graph indicates uniform steady pressure throughout the droplet at steady-state. It is worth noting that the dimensionless radius of the outermost particle is less than 1. This is because the plot shows $r^*$ at particle centres, which lie inside the radius $R$ defined in terms of 2D volume as

$$\mathrm{R} = \sqrt{\frac{V_0}{\pi}} \,, \tag{20}$$

where $V_0 = \sum_{i=1}^{N} V_i$ .

Results of a convergence study are shown in Figs. 6 and 7. Pressure error $\varepsilon_p$ decreases linearly as a function of dimensionless particle spacing $\Delta x^* = \Delta x / L$. This is expected, since neither particle centres nor particle common tangents

(used to approximate the direction of surface tension) lie exactly on the droplet circumference. This results in an error which converges as particle size is reduced and particle surfaces tend towards the true droplet surface.

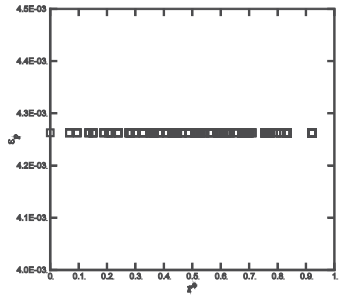

**Fig. 5.** Normalised error $\varepsilon_p$ between the numerical pressure and the Laplace analytical pressure, for all particles, as a function of $r^*$ (radial position of particles, normalized to final droplet radius) for 2D viscous droplet evolved from square configuration, $L/\Delta x$=25.

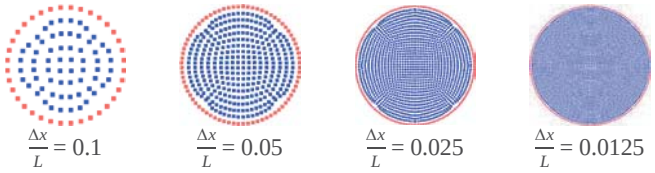


**Fig. 6.** Final states of initially square drop for various $\Delta x/L$ in a convergence study (red points are free-surface particles).

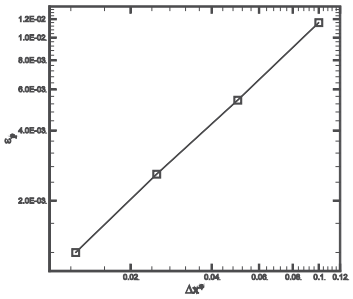

**Fig. 7.** Pressure error $\varepsilon_p$ (discrepancy between the numerical pressure and the Laplace analytical pressure, normalized to the analytical pressure) as a function of particle spacing.

The kinetic energy of the drop and its velocity field in steady-state condition are shown in Figs. 8 and 9. The maximum Mach number $M_{max}$ and dimensionless velocity $u^*$ are defined as $|\boldsymbol{u}|_{max}/c_0$ and $|\boldsymbol{u}|/(\sigma/\mu)$ respectively. The kinetic energy of the viscous drop dissipates faster than that of the inviscid drop. An infinitesimal value of fluid velocity and kinetic energy are remained in the numerical domain. Fig. 8 shows that when the Ohnesorge number increases the kinetic energy decreases. The effect of enhancement of Ohnesorge number is not only providing the smaller residual of kinetic energy but also smooth reduction of the kinetic energy. The solution shows that the final kinetic energy in the domain is very low. It is not classical parasitic velocity, but rather a rigid-body motion.

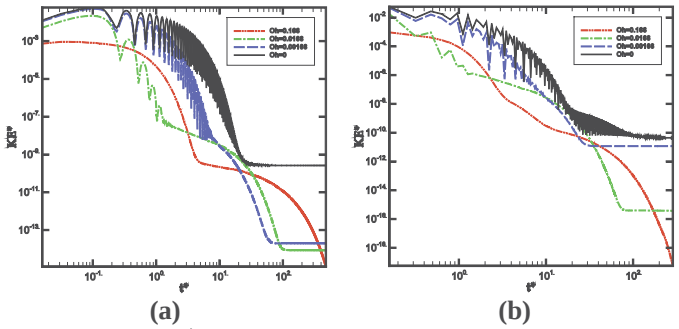

**Fig. 8.** Decay of $KE^* = KE/4L\sigma$ (kinetic energy normalized to initial surface energy) as a function of $t^*$ (time normalized to period of droplet oscillation) for 2D viscous droplet evolution from square configuration for various Ohnesorge numbers. (a) $L/\Delta x$=25 and $M_{max}$=0.034, (b) $L/\Delta x$=10 and $M_{max}$=0.074.

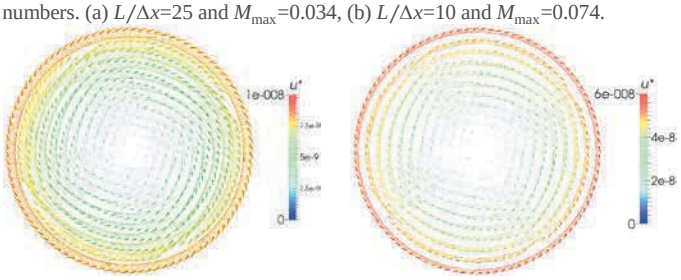

**Fig. 9.** Steady-state velocity field of 2D viscous liquid droplet after evolution from an initial square shape, $L/\Delta x$=25. (a) $Oh$=0.00166, (b) $Oh$=0.0166.

## B. *Oscillation of Perturbed Droplet*

The droplet was deformed from its final state in the last section to an elliptic configuration as the initial condition for a new test, following Nugent and Posch [2] and Yang *et al.* [19]. The deformation is applied using

$$\begin{pmatrix} x' \\ y' \end{pmatrix} = \sqrt{\frac{2}{\sin\varphi}} \begin{bmatrix} x\sin\left(\frac{\phi}{2}\right) \\ y\cos\left(\frac{\phi}{2}\right) \end{bmatrix}, \qquad (21)$$

where $\phi = e\pi$, and $x'$ and $y'$ are new values of $x$ and $y$. The value of $e$ (eccentricity) is 0.55. Figs. 10 and 11 show the oscillating deformation of the surface the drop. In these figures, $R^*$ is the dimensionless deformation parameter defined as $\sum_{i=1}^{N_{FS}} |\mathbf{x}_{i,FS} - \bar{\mathbf{x}}| / (R N_{FS})$, and $\mathbf{x}_{i,FS}$ and $N_{FS}$ are the positions and number of free-surface particles. In the deformation of the droplet surface, the effect of viscosity is evident, leading to faster damping of oscillations. The computed period of droplet oscillation, as shown in Fig. 10, is in close agreement with the theoretical value given by (18).

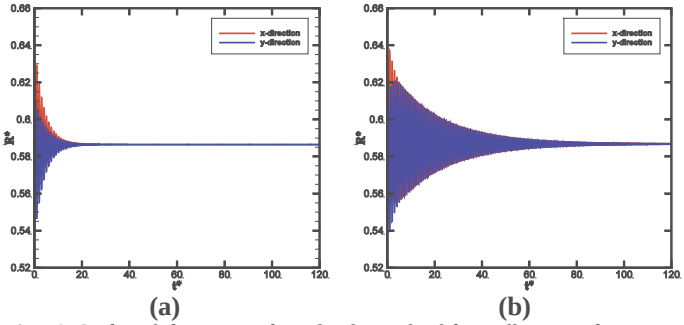

**Fig. 10.** Surface deformation of 2D droplet evolved from elliptic configuration versus time: (a) viscous and (b) inviscid.

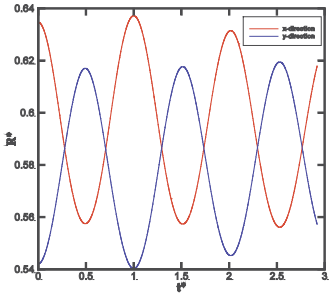

**Fig. 11.** Three cycles of Surface deformation of 2D inviscid drop evolved from elliptic configuration versus time.

Kinetic energy of the drop is shown in Fig 12. The strong surface tension at the poles of the perturbed droplet leads to intense oscillation in kinetic energy. In the viscous drop the energy dissipation is faster than the inviscid drop. Fig. 13 shows uniform pressure throughout the drop at equilibrium state.

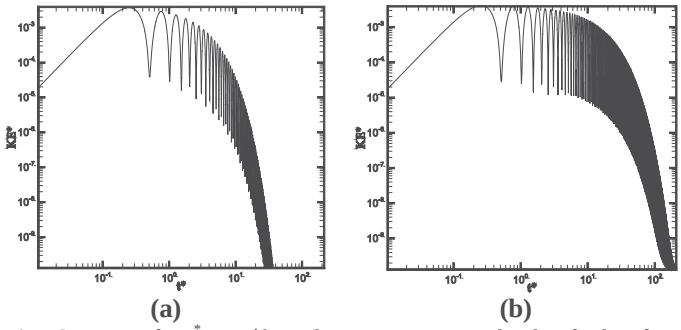

**(a)** **(b)**

**Fig. 12.** Decay of $KE^* = KE/2\pi R\sigma$ (kinetic energy normalized to final surface energy) as a function of $t^*$ (time normalized to period of droplet oscillation) for 2D droplet evolved from elliptic configuration: (a) viscous and (b) inviscid.

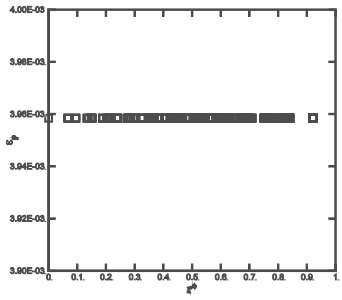

**Fig. 13.** Normalised error $\varepsilon_p$ between the numerical pressure and the Laplace analytical pressure, for all particles as a function of $r^*$ (radial position of particles, normalized to final droplet radius) for 2D viscous droplet evolved from elliptic configuration.

## C. *Liquid Drop on a Solid Wall*

In this section, the results of droplet formation from an initial square arrangement of particles on hydrophilic ($\theta_e$=80$^o$) and hydrophobic ($\theta_e$=110$^o$) solid surfaces are presented (Fig. 14). The ratio $L/\Delta x$ is 50. On the hydrophilic surface (Fig. 14(a)), the base of the droplet extends on the solid surface to increase the contact surface between the wall and the liquid, while in the hydrophobic case (Fig. 14(b)), the contact surface between the liquid and the wall is decreased. The contact angles for two cases have been checked in the final condition using the coordinates of the particles near the wall (Fig. 3), and are in close agreement with the prescribed equilibrium contact angles. Fig. 15 shows the decay of the kinetic energy. The final kinetic energy is very low in the absence of rigid-body motion.

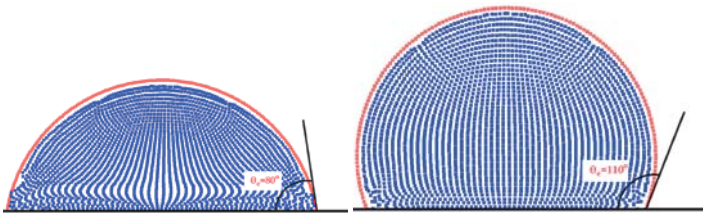

**(a)** **(b)**

**Fig. 14.** Viscous liquid drop in equilibrium state on hydrophilic (a) and hydrophobic (b) surfaces evolved from initial square configuration, , $L/\Delta x$=50 (red points are free-surface particles).

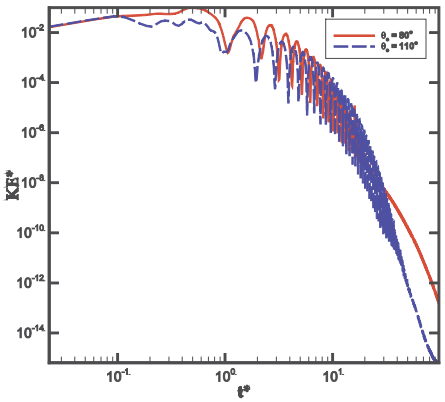

**Fig. 15.** Decay of $KE^* = KE/3L\sigma$ (kinetic energy normalized to initial surface energy) as a function of $t^*$ (time normalized to period of droplet oscillation) for a 2D viscous droplet on hydrophilic ($\theta_e$=80$^o$) and hydrophobic surfaces ($\theta_e$=110$^o$).

## D. *Impact of Small Cylinder on a Liquid Surface*

In this section, the new method is used to simulate a strongly dynamic, approximately two-dimensional experiment with strong surface tension effects. Vella *et al.* [20] provide experimental data and an approximate analytical solution for impact of a horizontal cylinder on a liquid free surface. In the experiment, the terminal velocity is much higher than the impact speed of the cylinder, so that aerodynamic forces can be neglected. The cylinder is released from rest and impacts with velocity $U$. The impact Froude number is defined as

$$F = \frac{U}{(gl_c)^{1/2}}, \qquad (22)$$

where $l_c = \sqrt{\sigma/\rho g}$ is the capillary length. The dimensionless radius $R$ and weight $W$ are defined as $r/l_c$ and $\pi r^2 \rho_s g/\sigma$ respectively. The parameters $r$ and $\rho_s$ are the radius and density of cylinder respectively. The experiment was carried out with water and isopropanol-water mixtures. The Reynolds number based on the diameter of the cylinder and the maximum velocity for floating varies between 151 and 322. The ratio $2r/\Delta x$ is 16.

Test conditions and results are shown Fig. 16 for the experimental and analytical results of Vella *et al.* and the present FVPM method. FVPM results for the boundary between sinking and floating regimes are close to both analytical calculations and experiments in the lower range of weight. At higher weight, FVPM and analytical models are in

good agreement, but both predict lower critical Froude number for sinking than observed in experiment. Vella *et al.* [20] suggested that, the differences between the experiment and the 2D analytical model may be due to surface tension force at the ends of the body, which can increase deceleration and allow the body to float for higher impact velocity. The end effects are also absent from the present 2D computational model, and may explain the discrepancy from experiment. Snapshots of the cylinder motion are presented in Fig. 17. It is seen that after downward motion the cylinder rebounds upward until it floats on the surface of the liquid.

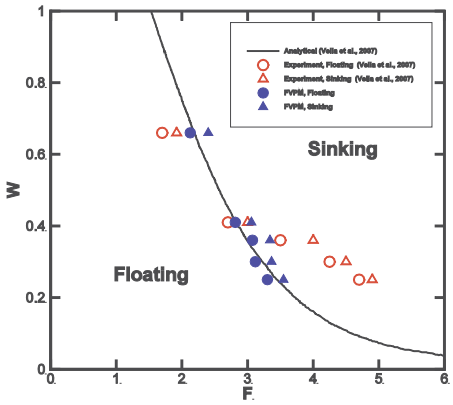


**Fig. 16.** Floating-sinking regime diagram of cylinder impact on a liquid surface.

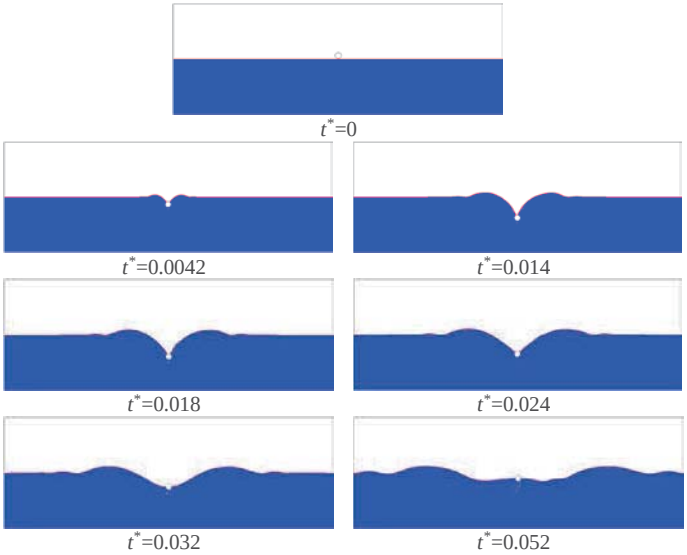


**Fig. 17.** Snapshots of the motion of a circular cylinder with $Re$=220, $F_F$=3.075, $F_S$=3.342, and $W$=0.36 (red points are free-surface particles).

## V. CONCLUSION

A new model for surface tension in the finite volume particle method (FVPM) has been presented in this paper. The new approach simplifies the surface tension implementation in comparison to the current methods. It has been tested for 2D static and dynamic liquid flows. The results obtained are in good agreement with analytical and experimental benchmarks. In static tests, drops reach equilibrium states with uniform pressure practically free of spurious velocity. Final kinetic energy (as a fraction of surface energy) is as low as $10^{-10}$ for a free inviscid droplet, $10^{-14}$ for a free viscous droplet with higher resolution, and $10^{-11}$ to $10^{-19}$ for a free viscous droplet with lower resolution. The residual kinetic energy appears not to be due to classical parasitic current, but a rigid-body motion of the whole drop. The normalised kinetic energy falls below $10^{-12}$ to $10^{-15}$ for a viscous droplet on a solid wall, in the absence of rigid-body motion, and the prescribed equilibrium contact angle is recovered. In simulations of cylinder impact on a liquid surface, predictions of floating or sinking outcome are in agreement with experimental data. All simulations were carried out with purely Lagrangian particle transport, and equilibrium was achieved despite notably non-uniform particle distribution in some cases. The only input parameters required are surface tension coefficient and equilibrium contact angle.

## ACKNOWLEDGEMENT

This publication has emanated from research conducted with the financial support of Science Foundation Ireland (SFI) and Aerogen®, and is co-funded under the European Regional Development Fund under Grant Number 13/RC/2073.

## REFERENCES

[1] D. Hietel, K. Steiner, and J. Struckmeier, “A finite volume particle method for compressible flows,” Mathematical Models and Methods in Applied Sciences, vol. 10, no. 9, pp. 1363-1382, 2000.

[2] S. Nugent and H. Posch. Liquid drops and surface tension with smoothed particle applied mechanics. *Physical Review E* 62: pp. 4968-4975, 2000.

[3] Y. Melean and L. Sigalotti. Coalescence of colliding van der Waals liquid drops. *International Journal of Heat and Mass Transfer* 48: pp. 4041-4061, 2005.

[4] A. Tartakovsky and P. Meakin, “Modeling of surface tension and contact angles with smoothed particle hydrodynamics,” Physical Review E, vol. 72, no. 2, p. 026301, 2005.

[5] J. Brackbill, D. Kothe, and C. Zemach. “A Continuum Method for Modeling Surface Tension,” *Journal of Computational Physics* 100: pp. 335-354, 1991.

[6] J. Morris. Simulating surface tension with smoothed particle hydrodynamics. *International Journal for Numerical Methods in Fluids* 33: pp. 333-353, 2000.

[7] M. Muller, D. Charypar, and M. Gross. Particle-Based Fluid Simulation for Interactive Applications. In: D. Breen and M. Lin (ed.), *Eurographics/SIGGRAPH Symposium on Computer Animation*. 2003.

[8] M. B. Liu and G. R. Liu. “Meshfree particle simulation of micro channel flows with surface tension,” Computational Mechanics, vol. 35, pp. 332-341, 2005.

[9] S. Adami, X. Hu, and N. Adams. A new surface-tension formulation for multi-phase SPH using a reproducing divergence approximation. *Journal of Computational Physics* 229: pp. 5011-5021, 2010.

[10] T. Breinlinger, P. Hashibon, and T. Kraft. Surface tension and wetting effects with smoothed particle hydrodynamics. *Journal of Computational Physics* 243: pp. 14-27, 2013.

[11] D. Schnabel and P. Eberhard. Study on Coarse-Fine-Interactions with an Adaptive SPH Formulation within the Context of Problems Driven by Surface Tension. In: X. Hu (ed.), *11th international SPHERIC workshop*. Technical University of Munich, Munich, Germany, 2016.

[12] A. Maertens, E. Jahanbakhsh, and F. Avellan. A Spherical Kernel for the Finite Volume Particle Method and Application to Surface Tension. In: X. Hu (ed.), *11th international SPHERIC workshop*. Technical University of Munich, Munich, Germany, 2016.

[13] A. Maertens, E. Jahanbakhsh, and F. Avellan. “A novel approach to surface tension modeling with the Finite Volume Particle Method,” Computer Methods in Applied Mechanics and Engineering, 2018 [Online]. Available: https://www.sciencedirect.com/science/article/pii/S0045782518300896

[14] M. S. Liou. “A sequel to AUSM: AUSM+,” Journal of Computational Physics, vol. 129, no.2, pp. 364–382, 1996.

[15] R. M. Nestor, M. Basa, M. Lastiwka, and N. J. Quinlan. “Extension of the finite volume particle method to viscous flow,” Journal of Computational Physics, vol. 228, no. 5, pp. 1733–1749, 2009.

[16] N. Quinlan, L. Lobovsky, and R. Nestor. Development of the meshless finite volume particle method with exact and efficient calculation of interparticle area. *Computer Physics Communications* 185:1554-1562, 2014.

[17] P.G. de Gennes, F. Brochard-Wyart, and D. Quere. Capillarity and wetting phenomena: Drops, Bubbles, Pearls, Waves. Springer, New York, 2002.

[18] Rayleigh L. On the capillary phenomena of jets. Proc R Soc London 1879;29:71-97.

[19] X. Yang, M. Liu, and S. Peng. “Smoothed particle hydrodynamics modeling of viscous liquid drop without tensile instability,” Computers & Fluids, vol. 92, pp. 199-208, 2014.

[20] Vella D. and Metcalfe P. D. Surface tension dominated impact. Physics of Fluids, vol. 19, pp. 072108, 2007.